PHOTOIONIZATION OF DISK WINDS

N. MURRAY[1] AND J. CHIANG[2]
Canadian Institute for Theoretical Astrophysics, University of Toronto, Toronto, Ontario M5S 3H8, Canada

ABSTRACT

The disk-wind model suggests that the broad emission lines of a quasar are emitted from the surface of the accretion disk feeding the central black hole. In this paper, we assume that a line-driven wind emerges from the illuminated face of the disk and calculate the line emission produced by this wind. The location and mass-loss rate of the wind are determined by the physics of the line driving. We calculate line ratios and the radius at which each line forms using a photoionization code. From the source functions, together with simple wind–radiative transfer calculations, we then calculate line profiles. The model reproduces the observed line ratios with a degree of success comparable to standard "cloud" models, underpredicting the flux in low-ionization lines and in N v $\lambda1240$. Using C IV to fix all the model parameters except for the line ratios, we find that the model successfully predicts the variety of line profiles seen in two PG quasars. We also present line profiles for Ne VIII that are very broad (FWHM $\sim$ 17,000 km s^{-1}) and predict that Mg X, while unlikely to be seen in emission, will be seen in absorption (in broad absorption line quasars). As suggested by previous authors, we find that the very broad feature seen around $\lambda2800$ and usually attributed to Mg II is actually a blend of that line, which is relatively narrow, and Fe II emission.

Subject headings: accretion, accretion disks — line: formation — quasars: general — radiative transfer

1. INTRODUCTION

Active galactic nuclei (AGNs) are believed to be powered by accretion onto black holes. Matter falls onto the hole through an accretion disk, in the process converting gravitational potential energy into the continuum emission, or light, that we observe. In fact, AGNs belong to a much larger class of objects believed to be accreting material through a disk onto a compact object. Other members of the class include cataclysmic variables, protostars, and X-ray binaries. It is also generally accepted that the continuum emission in AGNs is responsible for ionizing material in the vicinity of the disk and for powering the line emission that is one of the primary indicators of nuclear activity. For example, the narrow forbidden line emission seen in Seyfert galaxies is produced by low-density gas located tens to hundreds of parsecs from the central black hole. This gas is probably distributed in a roughly spherically symmetric form, although it may be illuminated by the central disk only in biconical regions.

In contrast to the narrow-line gas, the broad X-ray Fe K-line emission in AGNs comes from dense gas very near the black hole on the surface of the accretion disk (Tanaka et al. 1995; Iwasawa et al. 1996). The very large line widths may be produced by the Keplerian motion of the disk material. The spectacular observations of the H_2O megamaser in NGC 4258 show that this emission also comes from the illuminated surface of the accretion disk at large radii (Miyoshi et al. 1995; Herrnstein, Greenhill, & Moran 1996). In this case, the disk is well resolved so the lines are not broad, but the individual maser spots are clearly undergoing Keplerian motion.

Other examples of broad-line emission from the surface or wind of a self-illuminated accretion disk include the X-ray binary Her X-1 (Boronson et al. 1996), FU Orionis

stars (Welty et al. 1992), and cataclysmic variables (Young, Schneider, & Shectman 1981; Murray & Chiang 1996). The lines in cataclysmic variables come in two forms, double-peaked lines in low-luminosity cataclysmics (dwarf novae) and single-peaked lines in high-luminosity cataclysmics (nova-like variables and classical novae). Murray & Chiang argue that one difference between the two cases is that high-luminosity disks possess outflowing winds, as evidenced by P Cygni profiles in the C IV line, while low-luminosity disks do not. Radiative transfer effects in the wind produce emission that is much stronger along the wind-velocity gradient, leading to single-peaked profiles in some lines, such as He II $\lambda4686$.

The most spectacular broad emission lines are those seen in luminous AGNs. The standard story is that the emission is caused by large numbers of very small, dense "clouds" of photoionized gas at moderate (10,000–100,000 K) temperatures (Blandford, Netzer, & Woltjer 1990). Typical estimates of the cloud size, density, and filling factor (the fraction of the volume filled with clouds) are 10^{13} cm, $n \sim 10^{10}$ cm^{-3}, and 10^{-12}. The estimated size of the region producing broad emission lines is about 10^{18} cm in quasars, with smaller estimates applying to less luminous AGNs such as Seyfert galaxies. The full width at zero intensity of a typical broad line is $\gtrsim 20,000$ km s^{-1}, so the dynamical time in the broad-line region is about 20 yr. The sound crossing time of a single cloud is only a few months, leading to the "confinement problem": unless they are confined, clouds will dissipate before they can be accelerated to high velocity.

The observation of P Cygni profiles (called broad absorption lines) in 10% of radio-quiet quasars establishes the existence of outflowing gas. This gas is estimated to cover about 10% of the sky, suggesting that most or all radio quiet quasars have such outflows. Similar profiles are seen in Her X-1, the FU Orionis stars, and nova-like variables. In all these galactic sources, the outflow is believed to take the form of a wind emerging from the accretion disk. Murray et al. (1995; hereafter MCGV) have argued that the broad absorption lines in quasars also arise in a disk wind.

[1] murray@cita.utoronto.ca.
[2] Present address: Naval Research Laboratory, Code 7653, 4555 Overlook Avenue, Washington DC 20375.

In light of the evidence for line emission from self-illuminated disks and winds in so many different types of accretion-powered systems, it makes sense to consider the possibility that broad emission lines in AGNs form in a similar manner. The fact that cloud models suffer from the confinement problem only strengthens the argument. In this paper, we assume that the broad emission lines in all luminous AGNs form either in a disk wind or on the surface of the disk itself. This entails the assumption that AGN disks are self-illuminated, as are the disks in galactic accretion-disk systems.

This paper is organized as follows. In § 2 we describe the photoionization model, including the illumination of the disk and the variation of density in the wind and disk atmosphere. We assume that the flux striking the outer parts of the AGN disk varies with radius according to a simple broken power law and that there is a disk wind of the form described in MCGV. The line emission is then calculated using CLOUDY (Ferland 1993). In § 3 we describe the results of our CLOUDY runs in the form of line ratios and line source functions. Using the line source functions, we calculate line profiles and compare them to observed profiles. We give special attention to very high ionization lines (Mg x and Ne viii) and very low ionization lines (Mg ii). In § 4 we discuss previous photoionization calculations, as well as the reverberation mapping evidence bearing on the location of the Mg ii emission. In § 5 we give our conclusions.

2. PHOTOIONIZATION MODEL FOR DISK WINDS

We employ the photoionization code CLOUDY for all our photoionization calculations. The photoionization state of the gas depends on the spectral energy distribution and number density n_γ of ionizing photons in the radiation illuminating the gas. The photon number density is defined as

$$n_\gamma \equiv \frac{1}{c} \int_{\nu_0}^{\infty} \frac{F_\nu}{h\nu} \, d\nu \, , \qquad (1)$$

where ν_0 is the frequency at the Ly edge. The photoionization state of the gas depends as well on the metallicity and number density n of the gas. We use solar metallicity in our CLOUDY runs. The ionization parameter $U \equiv n_\gamma/n$ is a convenient way to describe a photoionized gas. If U is large compared with unity, the gas tends to be in a high ionization state, while if U is small, low–ionization state ions dominate the gas.

2.1. Illumination of the Disk

We assume that a substantial fraction of the energy emitted by the inner part of an AGN's disk strikes the outer disk. This will produce a temperature inversion or chromosphere in the outer disk, leading to line emission. Disk photospheres in luminous cataclysmic variables apparently flare [$z(r) \sim r^\alpha$ with $\alpha > 1$], so that radiation from the inner part of the disk strikes the outer disk (Marsh & Horne 1990]. The thin disk models of Shakura & Sunyaev (1973) are flat at small radii but flare at large radii, suggesting that the flux striking the inner disk should actually be smaller than the flux striking the outer disk. This conclusion is uncertain because the radiation pressure–dominated inner disk solution is unstable. To explore the possible effects of such flaring in our models, we adjust the flux striking the disk as a function of radius so that $F_{in} \sim 1/r^2$ for $r < r_{break}$ and $F_{in} \sim 1/r^\sigma$ for $r \geq r_{break}$. We have run models with σ

between 2 and 3. We have also explored models where the flux striking the disk decreases less rapidly than $1/r^2$ for $r < r_{break}$ with similar results for the line emission, namely that it increases rapidly at small radii, peaks near r_{break}, and then decreases. The line flux is an increasing function of r for very small r because the gas is too highly ionized at such small radii to produce line emission efficiently. Because there is little emission at small r, the actual form of F_{in} at small radii is not important. For this reason, in the following we restrict our attention to models with $F_{in} \sim 1/r^2$ for $r < r_{break}$. We choose the mass of the central black hole to fit the observed full width at zero intensity (FWZI) of the C iv line and choose r_{break} to fit the flux of Lyα assuming a covering factor of $f = 10\%$. The total amount of accretion luminosity absorbed and reradiated by the outer disk will depend on both the amount of flaring and the outer radius of the illuminated disk. Observations of the distribution of Balmer line emission from the surfaces of the secondary stars in nova-like variables shows that the disk in such systems covers a fraction $f \sim 10\%$ of the sky when viewed from the inner regions of the disk (Beuermann & Thomas 1990). We could treat either the cover factor of AGN disks or r_{break} as a free parameter; we have chosen to fix $f = 10\%$ and to vary r_{break}.

The angle at which radiation from the center of the disk strikes the disk is also not well constrained, since it depends on the amount of flaring. We have made runs where the incident radiation strikes the disk at an angle that depends on radius, as well as runs where the angle is fixed at various values. We show below that increasing the angle allows more radiation to penetrate to higher density, increasing the flux emitted by low–ionization potential ions (such as Mg ii) relative to that of high–ionization-potential ions (such as O vi).

The spectral energy distribution striking the disk in most of our models is that described in Mathews & Ferland (1987), with the X-ray portion of the spectrum modified to reflect the properties of radio-quiet quasars as described in MCGV. We run some models for the Seyfert galaxy NGC 5548 using the continuum in Krolik & Kriss (1996). The flux reaching the base of the wind may pass through a dense layer of "hitchhiking gas" at the inner edge of the line-emitting region (see MCGV). We have made runs both with and without filtering the central source through such a layer; the results do not depend strongly on the presence or absence of the hitchhiking gas. Recent observations of the far-UV continuum (Zheng et al. 1997) suggest that the Mathews & Ferland spectrum is rising too rapidly in that portion of the spectrum. We defer a description of our studies of the effect of altering the spectral energy distribution to a later publication.

2.2. Density as a Function of Position in the Wind

CLOUDY requires the density as a function of depth in the wind. Here we describe our model for the density distribution as a function of (r, z). We assume that an azimuthally symmetric line-driven wind emerges from the disk and accelerates outward. We further assume that the wind covers about 10% of the sky as seen from the central source. We choose this number based on the fraction of quasars showing broad blueshifted absorption in the C iv resonance line. The flow timescale is longer than the recombination time, so we assume that the gas is in photoionization equilibrium. The density depends primarily on the non-
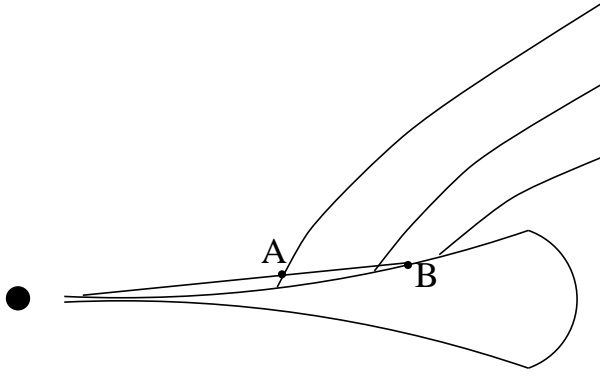
FIG. 1.—Cartoon of the geometry of a self-illuminated disk and wind. A line of sight from the center of the disk first meets the wind at the point marked "A" and strikes the surface of the disk proper at the point marked "B." The wind is shown on the upper surface of the disk only.

azimuthal component of the velocity. We assume that the nonazimuthal part of the velocity has a magnitude given by $v(r; r_f) = v_\infty(r_f)(1 - r_f/r)^\gamma + v_0$. The quantity r_f is the radius at which the streamline emerges from the disk. The terminal velocity of the flow is given by

$$v_\infty(r_f) \approx 4.7 \sqrt{\frac{GM_{bh}}{r_f}}, \qquad (2)$$

where M_{bh} is the mass of the central black hole (MCGV).

Given a wind model, we can solve for the footpoint $r_f(r, z)$ of the streamline passing through (r, z). We make the simplifying assumption that streamlines emerge from the disk at an angle λ and are straight. This is probably an adequate description of the flow at the rather low velocities where the bulk of the emission occurs. In that case, $r_f(r, z) = r - (z - z_0)/\tan \lambda$, where z_0 is the height of the disk at r. For simplicity we use $z_0 = 3\sigma_e L/(8\pi\eta c^3)$ at all radii. This is physically incorrect, but our numerical experi-

FIG. 2.—Run of density along a line of sight from the center of the disk to a point on the disk having a radius of $\approx 3 \times 10^{18}$ cm. The wind is that driven by a QSO with a luminosity of 10^{48} ergs s^{-1}, the luminosity of PG 1634+706. The corresponding line emission as a function of number density is shown in Fig. 3a.

ments suggest that the resulting line ratios and emissivities do not depend sensitively on the form of z_0. The density at the point (r, z) is then given by

$$n(r, z) = \frac{\dot{M}_w}{4\pi r^2 v[r, r_f(r, z)]m_p}. \qquad (3)$$

The mass-loss rate $\dot{M}_w$ in a line-driven wind is set primarily by the luminosity of the central source. In our dynamical models, the mass-loss rate was a significant fraction of L/cv_∞, which is the limit imposed by conservation of momentum in the single-scattering limit. In our CLOUDY models, we took the ratio $\dot{M}_w cv_\infty/L = \frac{1}{2}$.

Consider the line of sight indicated in Figure 1. Photons traveling along this line of sight first encounter the wind at A, with radius r_A, and are absorbed between this point and point B deep in the wind (or possibly in the disk proper). We start each CLOUDY run at A. The run is stopped when the column density exceeds 2×10^{25} cm^{-2} or when the temperature in the gas drops below either the temperature of the disk or the minimum allowed by CLOUDY (roughly $T = 3000$ K), whichever is larger. Generally, this is very near B. An example of the run of density in the wind is shown in Figure 2. This is part of our model for the luminous ($L \approx 10^{48}$ ergs s^{-1}) quasar PG 1634+706, described in more detail below. Most of the column density of the emitting gas is built up near B, where the density is large, as we show in the next section.

3. RESULTS OF CLOUDY RUNS

The photon number density n_γ decreases between points A and B in Figure 1. In contrast, the particle number density n increases by nearly 3 orders of magnitude, as shown in Figure 2, although that figure shows the density only near B. As a result, the ionization parameter $U \equiv n_\gamma/n$ is large at the inner edge of the wind and small near the surface of the disk, where most of the incoming radiation is absorbed and reemitted.

Figure 3 shows the line emission for several lines as a function of density along two lines of sight striking the disk. The ionization parameter is given by the axis running along the top of the figure. In Figure 3a, the line of sight strikes the disk at $r_B \approx 3 \times 10^{18}$ cm (the corresponding run of density is given in Fig. 2) while in Figure 3b, $r_B \approx 3 \times 10^{19}$ cm. We have chosen a bolometric luminosity of 3×10^{48} ergs s^{-1}, appropriate for the quasar PG 1634+706. In both cases, the cumulative line emission is dominated by Lyα and, to a lesser extent, by C IV. This emission occurs in the low velocity ($v \lesssim 10^7$ cm s^{-1}) part of the wind very near the surface of the disk at the point B in Figure 1. Higher above the disk, where the wind is less dense and the ionization parameter is high, the emission is biased toward high-ionization species such as Ne VIII and O VI. As the column builds up, the incoming radiation is gradually absorbed, eventually causing the emission to cease. Just before this occurs, low-ionization species such as Mg II begin to emit. The amount of Mg II emission is very small in Figure 3a since the incoming radiation is essentially completely absorbed when $U = 100$. In Figure 3b, emission ceases at $U = 0.2$, so that the low-ionization lines are able to radiate more efficiently.

Similar behavior can be seen in Figure 1 in Baldwin et al. (1995). Those authors show contour plots of line emission as a function of $\Phi \equiv n_\gamma/c$ and n. Each panel in our Figure 3 represents a slice through the Φ-n plane shown in Figure 1
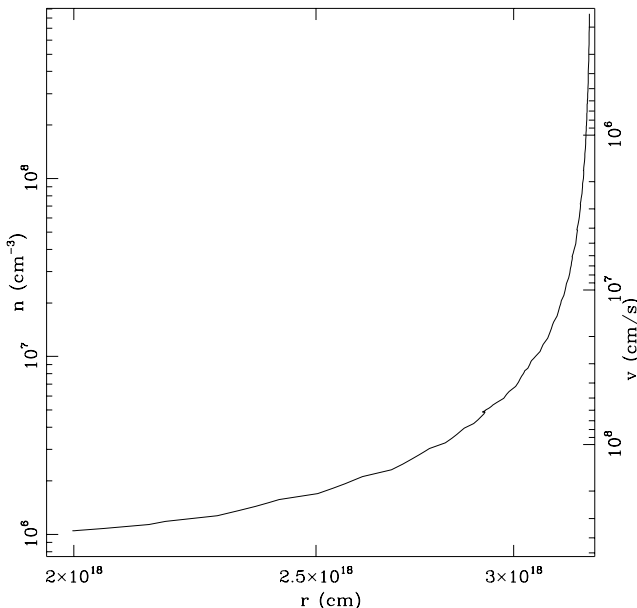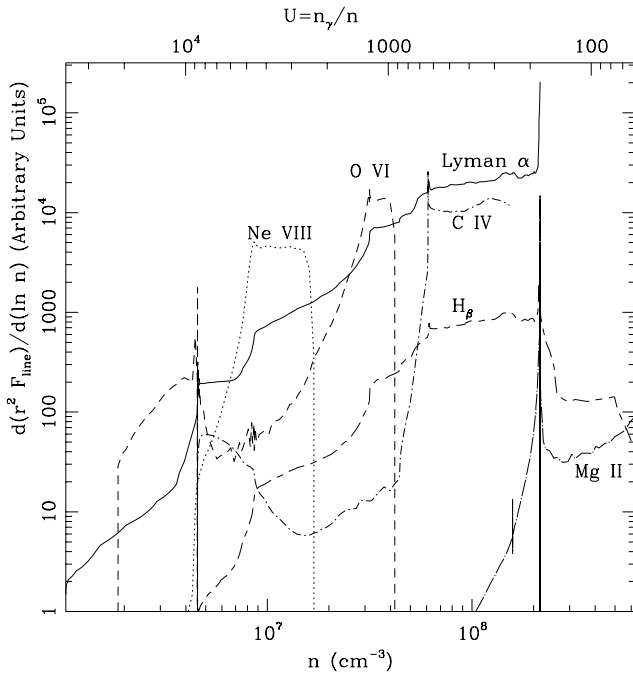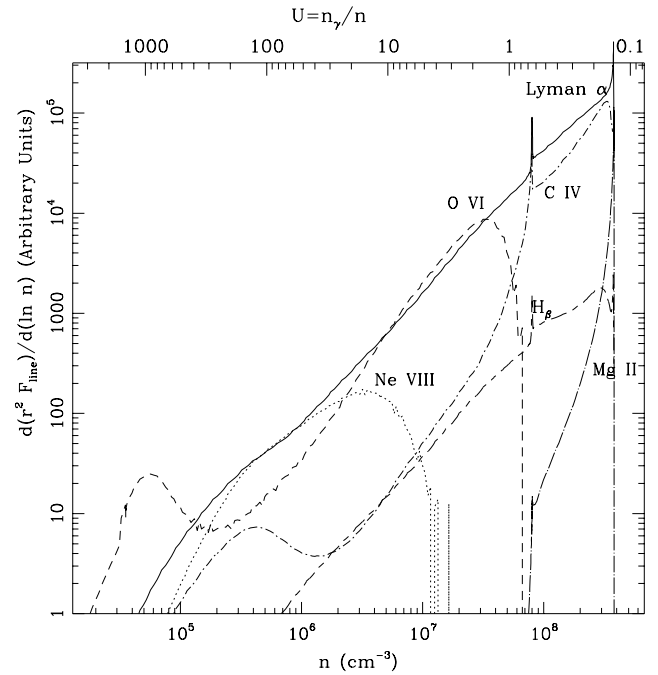
FIG. 3.—Line emission as a function of density along a line of sight that strikes the disk. The ionization parameter U, defined using the unabsorbed flux, is shown along the top of the figure. The solid lines correspond to Lyα, the dotted lines to Ne VIII, the short-dashed lines to O VI, the dot–short-dashed lines to C IV, the short-dash–long-dashed lines to Hβ, and the dot–long-dashed lines to Mg II. In (a) the line of sight strikes the disk at $r = 3.16 \times 10^{18}$ cm, while in (b) the line of sight strikes the disk at $r = 3.16 \times 10^{19}$ cm. The luminosity of the source is 3×10^{48} e s^{-1}. Note that in both cases, the higher ionization lines (e.g., Ne VIII and O VI) emit at larger U and smaller densities than do the low-ionization lines (e.g., Mg II). The high-ionization lines are emitted by gas having a substantial radial velocity. The run of density along the line of sight from the central disk for (a) is shown in Fig. 2.

of Baldwin et al. (1995). Moving from small r to large r through the wind, we move from left to right and slightly down in their Figure 1. Each metal ion tends to emit at a characteristic value of U. Examining their figure, we see that as r increases, O VI emission occurs first, followed by C IV, and finally Mg II (if the radiation penetrates to high enough density, as in Fig. 3b). As the line of sight approaches the disk, the ionizing photons begin to be absorbed, so that the locus of points traced out in the Φ-n plane eventually drops vertically, and line emission ceases.

The line AB makes an angle α with the disk surface at B. We assume that $\alpha \lesssim 0.1$ over the range of radii where the line emission occurs. Thus the optical depth along AB is much larger than the optical depth from point B upward along the disk normal. CLOUDY assumes normal incidence ($\alpha = \pi/2$), so the actual column experienced by the emerging radiation is smaller by a factor of α than that employed by CLOUDY and, hence, in our calculations. Both the continuum and line optical depths are overestimated in our CLOUDY runs. Another difficulty with our use of CLOUDY in the context of a wind model is related to the code's simple treatment of radiative transfer. CLOUDY uses escape probabilities to calculate which line photons escape from and hence cool the gas, but the escape probabilities employed assume that the gas is static. Once again, the code overestimates the optical depth in the lines. We have not investigated the effect of using the proper, lower, line optical depths.

The overestimate of the continuum optical depth to escaping photons is not likely to alter the line profiles, although it may affect the line ratios. The incident radiation penetrates to a continuum optical depth of order unity. The

line photons that are subsequently emitted will see a continuum optical depth that is of order $\alpha \lesssim 0.1$ near the Lyman edge. Typically, the Thompson depth is much less than this, since the Lyman edge optical depth reaches unity well before the Thompson depth does; when the Lyman edge photons are all absorbed, the emission effectively ceases. The exception to this occurs at the inner edge of the emitting region where the Thompson depth along AB can reach or even slightly exceed unity. Here, the vertical Thompson depth might reach a few tenths; an example is shown in Figure 1 and Figure 3a. However, gas under these extreme conditions is not very efficient at producing line emission. The emission from this radius accounts for only a few percent of the total Lyα emission in this model. Most of the emission comes from larger radii, where the Thompson depth along AB is less than one tenth, while the vertical Thompson depth is less than 10^{-2}.

The fact remains that few percent of the line emission will be subject to Thompson scattering depths of order a few tenths. The electron temperature ranges up to 10^6 K, so a single scattering will move the photon 1000 km s^{-1} in velocity space. One percent of the emitted photons, shifted in velocity by 1000 km s^{-1}, will not appreciably affect the line profiles. However, the photons are shifted well out of resonance, so they will escape isotropically. This is in contrast to the bulk of the line photons, which escape anisotropically (see § 3.5). Photons emitted from regions of the disk with high projected velocities, which would not normally escape along our line of sight because of the anisotropic line optical depth, could broaden the line wings (at $\pm 10,000$ km s^{-1}). For lines such as Lyα or C IV $\lambda 1550$, this effect is negligible. However, the Ne VIII $\lambda 774$ line forms at

very small radii in our model. Given sufficiently high signal-to-noise ratio (S/N) spectra, the alterations in the line profile might be noticeable. An example is shown below. We also show below that low-ionization lines such as Mg II originate at large radii in a disk wind, so electron scattering is not important for these lines.

3.1. The Effect of Varying the Angle of the Incident Radiation

The angle between the incident radiation and the surface of the disk (or between the incident radiation and the wind streamlines) is uncertain. We have explored the effect of varying this angle. To understand the results, it is helpful to note that the photons along a particular line of sight will be absorbed by a column density that varies only slowly as the parameters of the wind and disk are varied. Suppose we decrease the angle between the incident radiation and the disk and hold the angle between the wind streamlines and the disk fixed. This will increase the path length through the wind to the surface of the disk. Since the column the incident photons can penetrate to is roughly fixed, these photons will be absorbed higher above the disk, where the wind velocity is larger. Consequently, the incident radiation is absorbed and reemitted in gas of lower density, increasing the ionization parameter at which the bulk of the emission occurs. As a result, we expect, and find, an increase in the flux emitted in high-ionization lines and a decrease in the flux emitted in low-ionization lines. Figure 4 illustrates our numerical results. In all three panels, the emission occurs at $r \approx 10^{18}$ cm. In Figure 4a, the radiation strikes the disk at an angle of 6°, while in Figure 4b the angle is 0°.6. The flux of Ne VIII relative to Lyα increases from 0.01 to 0.03 with the decrease in incident angle, while the flux of Mg II decreases from 0.01 to 0.005.

3.2. The Effect of Varying the Wind Mass-Loss Rate

The mass-loss rate of the wind is also uncertain. Increasing the mass-loss rate will increase the density of the wind at every point in the wind and at every velocity. This tends to decrease the ionization parameter at which the emission occurs. However, the velocity corresponding to the maximum column reachable by the incident photons is also increased. This tends to increase the ionization parameter at

which the emission occurs. The latter effect dominates, so the net result of increasing the mass-loss rate while holding all other parameters fixed is to increase the flux in high-ionization lines relative to that in low-ionization lines. This is illustrated in Figure 4c, which shows the emission in a model similar to that in Figure 4a, but with the mass-loss rate increased by a factor of 10. Increasing the mass-loss rate increases the Ne VIII flux from 0.01 to 0.02 times that of Lyα while decreasing the Mg II flux from 0.01 to 0.003.

3.3. Line Ratios

The line intensities (relative to Lyα) resulting from a set of generic calculations are presented in Table 1. Column (1) identifies the emission line/blend, column (2) gives the range of observed intensities, and columns (3), (4), and (5) are the calculated ratios for $\sigma = 3$, 2.5, and 2, where the incident flux scales as $F \sim 1/r^\sigma$ beyond r_{break}. The luminosity of the source is 10^{46} ergs s^{-1}. The covering fraction of the disk is taken to be independent of radius. The range of line intensity ratios is generally compatible with the observed ratios for the high-ionization lines, with the clear exception of N V. This is underpredicted, in agreement with other photoionization calculations that assume solar abundances (Baldwin et al. 1995; Hamann & Ferland 1993). The low-ionization lines also tend to be underpredicted, as for example Hβ and Si IV; once again, this is a longstanding problem with photoionization models. One clear difference from previous photoionization models is the rather small line ratio predicted for Mg II. This arises because the wind necessarily has only moderately high densities, and then only at very large columns. Cloud models are free to postulate very dense but low column clouds at large radii where the photon number density n_γ is small; under these conditions, much of the absorbed radiation is emitted in the form of Mg II photons. Many authors have noted that the Mg II λ2798 feature lies on top of a multitude of Fe II emission lines. We argue below on the basis of reverberation mapping results that the broad feature at $\lambda \sim 2798$ is likely to be caused by Fe II emission and that the actual strength of the Mg II emission is significantly smaller than is usually assumed. In our models, the bulk of the Mg II emission occurs at large radii, where the density in the wind is low because of the $1/r^2$ factor in equation (3). Our calculations

TABLE 1

Observed and Predicted Line Intensities

Emission Line (1)	Observed Intensity[a] (2)	$F \sim r^{-3}$ (3)	$F \sim r^{-2.5}$ (4)	$F \sim r^{-2}$ (5)
Ne VIII λ774	...	0.06	0.04	0.02
O VI λ1034 + Lyβ λ1026	0.1–0.3	0.18	0.14	0.08
Lyα λ1216	1.00	1.00	1.00	1.00
N V λ1240	0.1–0.3	0.03	0.02	0.02
Si IV λ1397 + O IV] λ1402	0.08–0.24	0.05	0.04	0.03
C IV λ1550	0.4–0.6	0.35	0.38	0.35
He II λ1640 + O III] λ1666	0.09–0.2	0.13	0.11	0.09
C III + Si III] + Al III λ1900	0.15–0.3	0.07	0.09	0.12
Mg II λ2798 + Fe II	0.15–0.3	0.01[b]	0.02[b]	0.05[b]
Hβ λ4861	0.07–0.2	0.02	0.02	0.02
O [III] λ4363	0.000–0.010	0.006	0.007	0.002
O [III] λ5007	0.000–0.015	0.005	0.005	0.001
Ne V λ3426	0.000–0.010	0.004	0.005	0.002
Fe XI λ7892	0.000–0.010	0.002	0.002	0.002

[a] Intensity relative to Lyα λ1216, taken from Baldwin et al. 1995 (allowed transitions) and Alexander & Netzer 1994 (forbidden transitions).
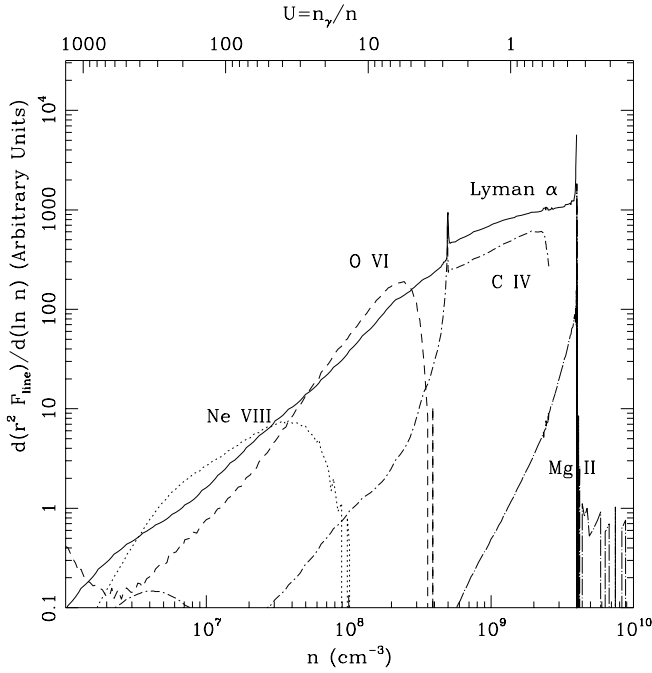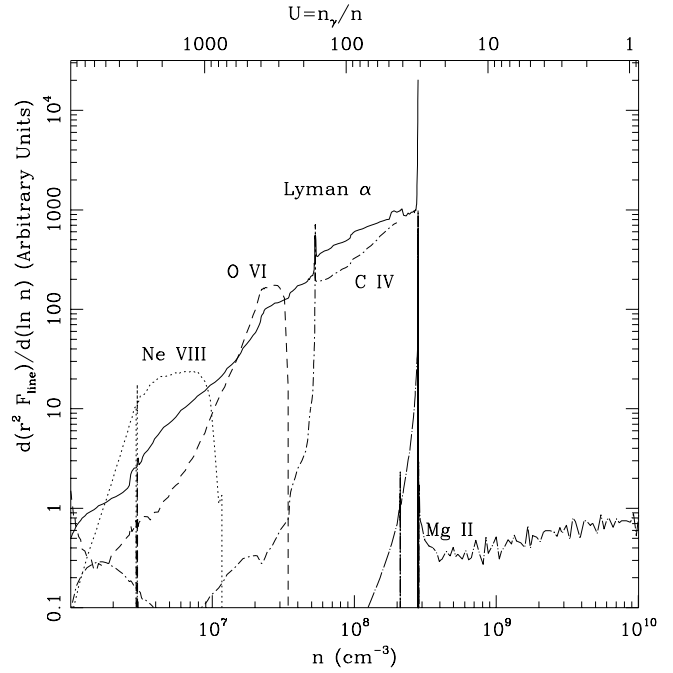[b] Intensity of the unblended Mg II component only.
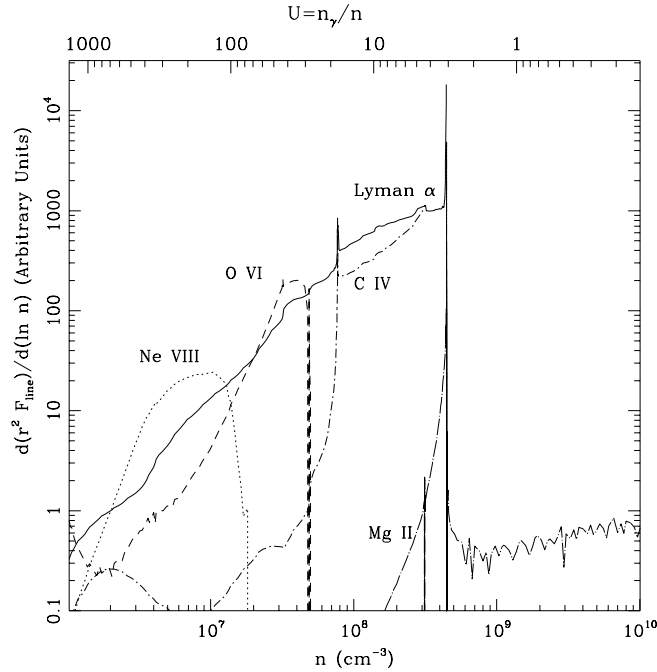
FIG. 4a

FIG. 4b

FIG. 4c

FIG. 4.—Line emission $r^2 dF_{line}/d(\ln n)$ for (a) incident radiation striking the disk at an angle of $6°$; (b) incident radiation at $0°.6$ and the same mass-loss rate; and (c) incident radiation at $6°$ but with a mass-loss rate 10 times that of the models shown in (a) and (b). The line style is as in Fig. 3, except that we do not plot the $H\beta$ emission. Decreasing the angle at which the radiation strikes the disk increases the ionization parameter U at which the lines are formed. Increasing the mass-loss rate also increases the ionization parameter at which the lines are formed.

show that the incident radiation penetrates below the sonic point in the wind; the Mg II emission is essentially coming from the surface of the disk rather than from the wind.

Comparisons with *Hubble Space Telescope* (*HST*) observations of two quasars are given in Tables 2 and 3 (PG 1116+215 and PG 1634+706, respectively), with the data in the second column taken from Laor et al. (1995). Laor et al. find a luminosity $L_{1350} \equiv \nu L_\nu = 1.5 \times 10^{48}$ ergs s^{-1} at

$\lambda = 1350$ Å for PG 1634+706, and $L_{1350} = 10^{46}$ ergs s^{-1} for PG 1116+215. The third column in each table gives the predicted line ratios for an illuminated disk model with the appropriate luminosity. The results are similar to the generic case, with N v and Mg II underpredicted. The flux in the He II complex is overpredicted. This may be caused by the spectral energy distribution that we employ, which appears to overpredict the far-UV continuum flux.

TABLE 2

PG 1116+215 LINE INTENSITIES

Emission Line	Observed Intensity[a]	$F \sim r^{-2.5}$
Ne VIII $\lambda774$	...	0.04
O VI $\lambda1034$ + Lyβ $\lambda1026$	0.20	0.14
Lyα $\lambda1216$	1.00	1.00
N V $\lambda1240$	0.17	0.02
Si IV $\lambda1397$ + O IV] $\lambda1402$	0.14	0.04
C IV $\lambda1550$	0.45	0.38
He II $\lambda1640$ + O III] $\lambda1666$	0.04	0.11
C III + Si III] + Al III $\lambda1900$	0.16	0.09
Mg II $\lambda2798$ + Fe II	...	0.02[b]

[a] Intensity relative to Lyα $\lambda1216$, taken from Laor et al. 1995.
[b] Intensity of the unblended Mg II component only.

Broad forbidden lines are conspicuous by their absence from quasar spectra. We include the broad-line strengths of four forbidden lines in Table 1, including only the emission at velocities above 500 km s^{-1}. We find essentially no forbidden emission in the broad-line region.

3.4. Line Source Functions

Our CLOUDY models tell us the run of vertically integrated line emission with disk radius. Figure 5 shows these line source functions for several prominent emission lines, assuming $L_{1350} = 10^{46}$ ergs s^{-1}. We assume $r_{break} = 10^{18}$ cm and $M_{bh} = 4 \times 10^8 \, M_\odot$, and we hold the angle between the line of sight from the central source to the point of emission constant at 6°; $\sigma = 2$, 2.5, and 3 in Figures 5a, 5b, and 5c, respectively. Inside r_{break}, we assume that the incident flux scales as $1/r^2$.

Inside r_{break}, the line emission increases rapidly with increasing r. This occurs because, at small radii, the emitting gas is too highly ionized to radiate in the lines or the lines are thermalized. Gas farther from the central source is subject to a smaller ionizing flux, and so produces line emission more efficiently. Beyond r_{break}, the total line emission scales with F_{in}, since we chose r_{break} large enough that most of the cooling occurs through line emission. Had we chosen r_{break} smaller, the general shape of the source functions would have been similar, but the total amount of line emission would have been smaller.

Inspection of Figure 5 reveals that the high–ionization line source functions generally peak at smaller radii than the low–ionization line source functions do. This suggests that the high-ionization lines should have broader profiles. In the next subsection, we show that this is indeed the case. They should also respond more rapidly to variations in the continuum, although we have not yet tried to quantify this

TABLE 3

PG 1634+706 LINE INTENSITIES

Emission Line	Observed Intensity[a]	$F \sim r^{-2.75}$
Ne VIII $\lambda774$	...	0.03
O VI $\lambda1034$ + Ly $\beta\lambda$ 1026	0.17	0.09
Lyα $\lambda1216$	1.00	1.00
N V $\lambda1240$	0.17	0.01
Si IV $\lambda1397$ + O IV] $\lambda1402$	0.09	0.03
C IV $\lambda1550$	0.28	0.40
He II $\lambda1640$ + O III] $\lambda1666$	0.02	0.10
C III + Si III] + Al III $\lambda1900$	0.12	0.13
Mg II $\lambda2798$ + Fe II	0.10	0.03[b]

[a] Intensity relative to Lyα $\lambda1216$, taken from Laor et al. 1995.
[b] Intensity of the unblended Mg II component only.

effect. We note that observations of Seyfert galaxies clearly show that the high-ionization lines respond more rapidly to changes in the continuum flux (Korista et al. 1995).

3.5. Line Profiles

Given the source functions, the monochromatic specific luminosity from a disk viewed at an angle i from the disk axis is (Horne 1995; Murray & Chiang 1997)

$$\mathscr{L}_\nu(\mathbf{n}) = \sum_{j=(+,-)} \int r \, dr \, S_\nu(r) \frac{l_{em}}{v_\phi}$$
$$\times \frac{|Q_j|\sqrt{1 + (l_{Sj}/l_{em})^2}}{\sin i \, |\cos \phi_j|} \left[1 - e^{-\tau_j}\right], \quad (4)$$

where

$$\tau_\pm = \left(\frac{k_0 c}{\sqrt{\pi}v_0}\right) \Big/ |Q_\pm| \sqrt{1 + \left(\frac{l_{S\pm}}{l_{em}}\right)^2}, \quad (5)$$

$l_S = v_{th} \cos i/|Q|$ is the Sobolev length, and $l_{em} \equiv v/(dv/dr)$ is the length scale in the wind. The emission at a specific frequency ν arises from a narrow locus of points on the surface of the disk given by the solution to the equation

$$\sin \phi_* \approx -\left(\frac{v - v_0}{v_0}\right) \frac{c}{v_\phi(r) \sin i}, \quad (6)$$

where v_0 is the frequency at line center and ϕ is the azimuthal angle on the disk, measured from the line of sight. There are two solutions to this equation for each (v, r) pair, which we denote by $\phi_\pm$. The quantity Q is the double-dot product of the strain tensor with the line-of-sight vector $\mathbf{n}$ from the point of emission on the disk to the observer. It is given by

$$Q = \sin i^2 \left[\frac{dv_r}{dr} \cos^2 \phi + \frac{v_r}{r} \sin^2 \phi + \left(\frac{3}{2}\right) \frac{v_\phi}{r} \sin \phi \cos \phi\right]$$
$$- \cos i \left[\frac{dv_r}{dr} (\sin i \cos \phi \cot \lambda + \cos i)\right.$$
$$\left. + \frac{v_\phi}{(2r \sin \lambda)} \sin i \sin \phi\right]. \quad (7)$$

The wind emission described by equation (7) is not isotropic. Line photons emerging from the disk escape preferentially along directions where the velocity gradients are large. Since dv/dr is substantially larger than v_ϕ/r in a line-driven wind (when $v > v_{th}$), photons tend to escape along the line $\phi = 0$ or 180. This ensures that the high-ionization lines are single peaked even though they form at small radii. This effect is weakened for Mg II, since some of the emission comes from gas moving below v_{th}. However, we find that Mg II is single peaked simply because it is emitted at such large radii (see § 4).

Figures 6 and 7 show the observed (*jagged solid line*; data from Laor et al. 1995) and calculated (*dotted line*) line profiles for PG 1116+215 and PG 1634+706. The total line flux, relative to Lyα, is given in Table 1. These predicted line ratios are close but not exactly equal to the observed line ratios, making it difficult to assess the agreement between the shapes of the observed and calculated profiles. To make the comparison easier, the smooth solid line in each figure shows the calculated line profile when the line ratio for each line is treated as a free parameter. The χ^2 for the smooth
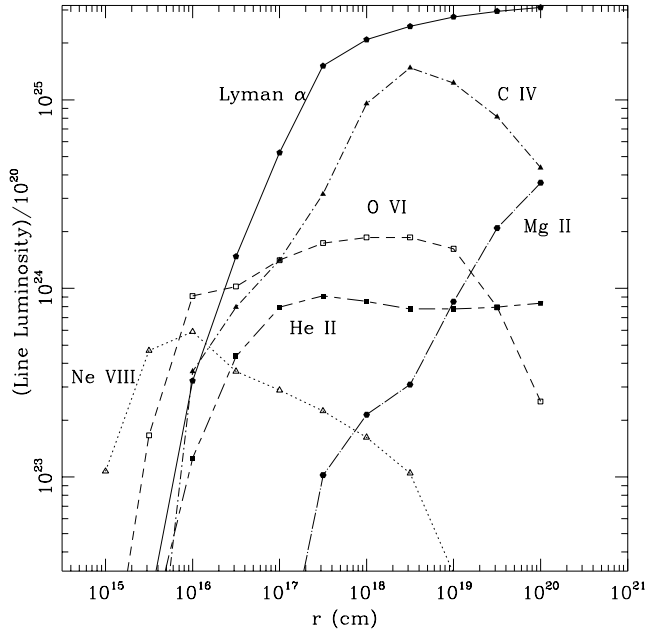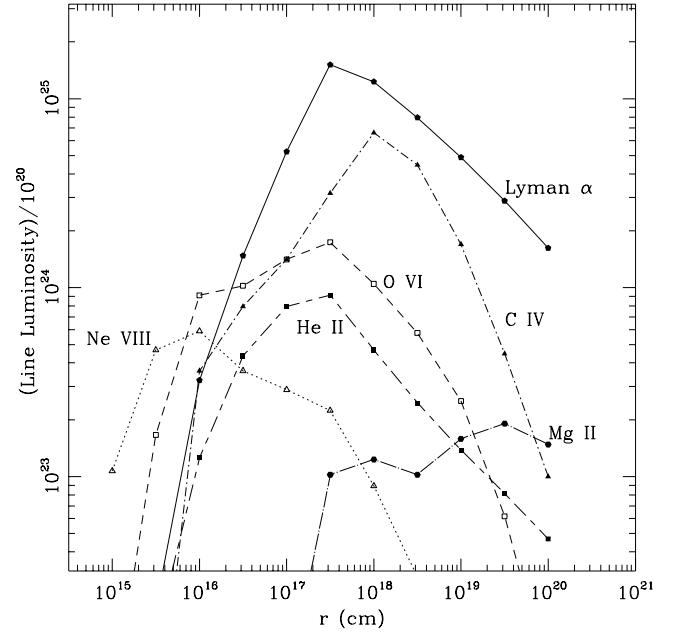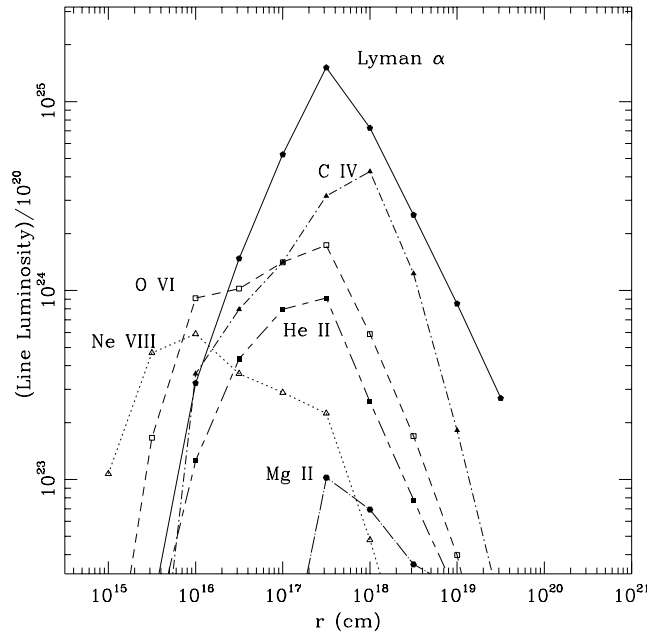
FIG. 5a

FIG. 5b

FIG. 5c

FIG. 5.—Line luminosity as a function of radius, assuming a constant cover factor [$f(r)$ = constant], for three different incident broken power laws: (a) $F_{\rm incident} \sim r^{-2}$; (b) $F_{\rm incident} \sim r^{-2}$ for $r < r_{\rm break} = 3 \times 10^{17}$ cm and $F_{\rm incident} \sim r^{-2.5}$ for $r \geq r_{\rm break}$; and (c) $F_{\rm incident} \sim r^{-2}$ for $r < r_{\rm break} = 3 \times 10^{17}$ cm and $F_{\rm incident} \sim r^{-3}$ for $r \geq r_{\rm break}$. The line style is as in Fig. 3, except that the short-dash–long-dashed lines now indicate the emission of He II rather than that of Hβ. Note that the peak emission for high-ionization lines occurs at smaller radii than the peak emission for low-ionization lines.

solid line profile and the number of points in the fit are shown in each panel.

In calculating the source function, the incident flux is taken to scale as $F \sim 1/r^{2.75}$ beyond $r_{\rm break} = 3 \times 10^{18}$ cm in the case of PG 1634+706 and $F \sim 1/r^{2.5}$ beyond $r_{\rm break} = 3 \times 10^{17}$ cm for PG 1116+215. These radii are chosen so that the luminosity in Lyα matches the observed luminosity, assuming a covering factor $f = 0.1$. The profiles are not particularly sensitive to $r_{\rm break}$ as long as it is not too large. If it is chosen so large that all the ions except hydrogen have ceased to emit (at about 10^{20} cm for $L_{1350} = 10^{46}$), the profiles are too peaky, so that if the line base has the proper

width, the line core is too broad (the FWHM is too large). If $r_{\rm break}$ is taken to be smaller than this, the shapes of the profiles are roughly independent of $r_{\rm break}$; the total line flux decreases with decreasing $r_{\rm break}$ (holding $M_{\rm bh}$ fixed).

The other adjustable parameter is the mass of the central black hole, which sets the FWZI for the lines. For PG 1634+706, we have taken $M_{\rm bh} = 4 \times 10^{10}\ M_\odot$, and for PG 1116+215, $M_{\rm bh} = 3 \times 10^{8}\ M_\odot$. These values were chosen to match the full width at zero intensity of the observed C IV profile by minimizing the χ^2 of the fit. We have not attempted to fit the line wings with great precision since the S/N of the data available to us do not warrant such an attempt. We
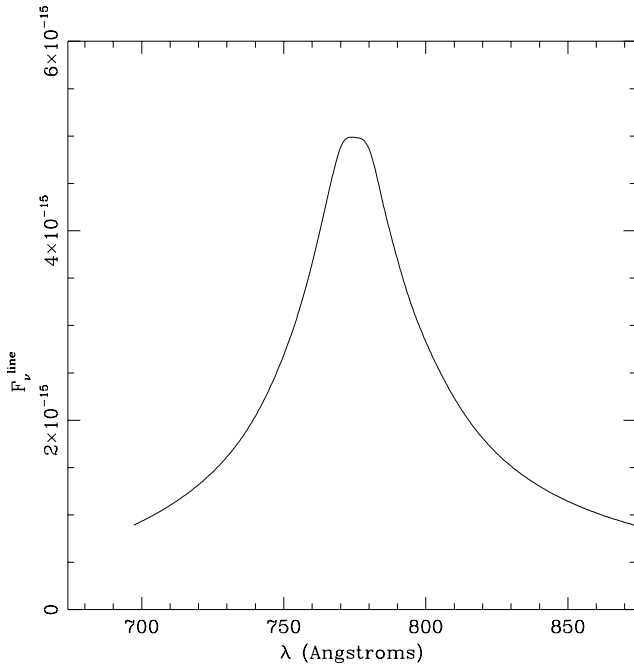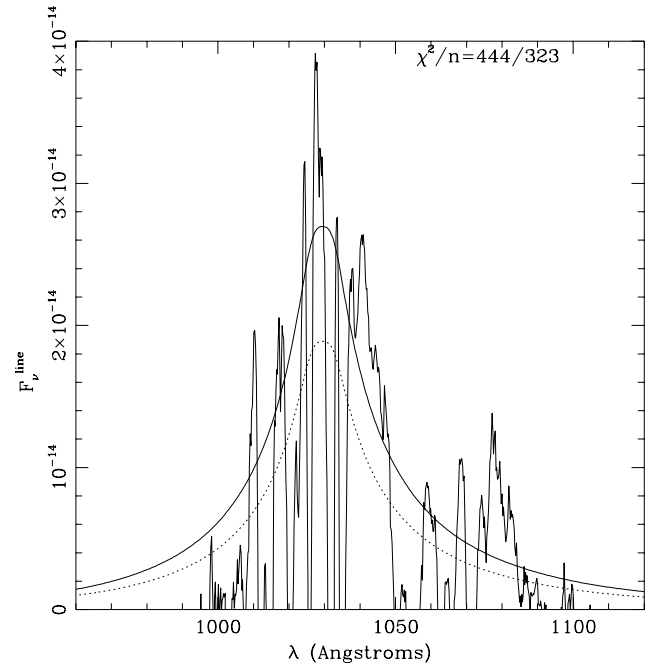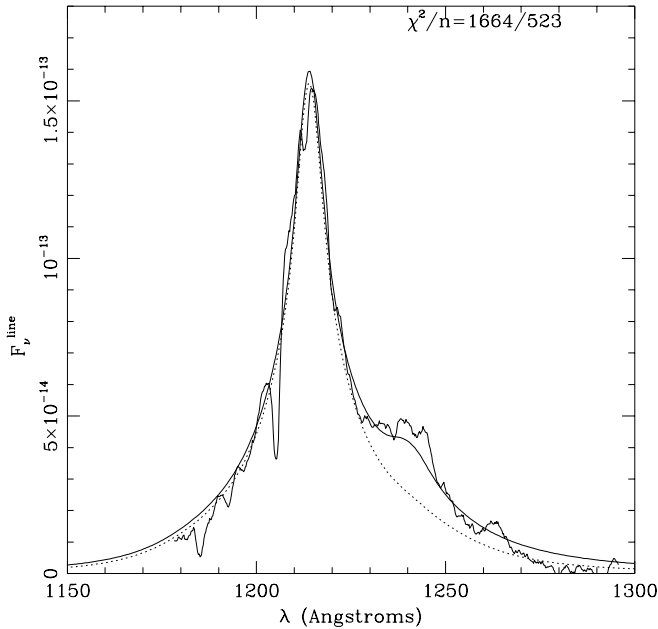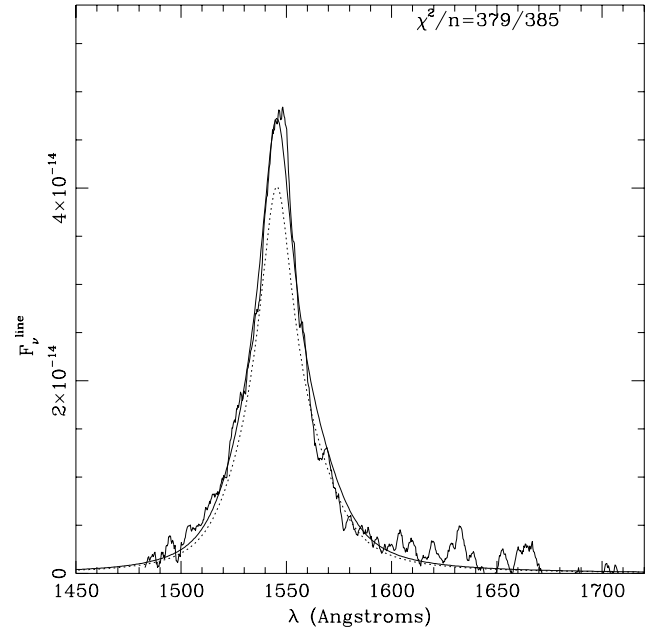
Fig. 6a

Fig. 6b

Fig. 6c

Fig. 6d

FIG. 6.—Line profiles generated by the source function shown in Fig. 5b (*dotted lines*), compared to the profiles observed in PG 1116+215 by Laor et al. (1995). The free parameters of the fit are the black hole mass ($3 \times 10^8 \ M_\odot$, fixed by the full width at zero intensity of the C IV line) and the break radius ($r_{break} = 3 \times 10^{17}$, set by the flux of the Lyα line, assuming a covering factor of 10%). The calculated flux in the Lyα and N V lines with these parameters is 476 and 101 (in units of $10^{-14} \ \mathrm{ergs^{-1} \ s^{-1} \ cm^{-2}}$), compared to 497 and 97 in the deblended result of Laor et al. In order to illustrate the fit between the line shape predicted by the model and the observations, we have also plotted profiles (*smooth solid lines*) in which the line ratios were treated as free parameters. The χ^2 and number of points in the latter fit is shown in each panel. The lines are (a) Ne VIII λ774, (b) O VI λ1035, (c) Lyα λ1215 + N V λ1240, (d) C IV λ1550, (e) C III] λ1909, and (f) Mg II λ2798.

can change the mass of the black hole by up to a factor of 2 (e.g., $2–8 \times 10^{10} \ M_\odot$ for PG 1634+706) and still obtain acceptable values of χ^2 for the C IV profile. The black hole mass for PG 1634+706 is very large but is consistent with the very large inferred luminosity.

Table 4 lists the parameters of the model, indicating those that were considered fixed and those that were varied to obtain the C IV line profiles shown in Figures 6 and 7.

Having fitted the C IV profile, we held fixed all parameters except the line fluxes in fitting the other profiles.

Referring to Figures 6 and 7, we see that we can easily find acceptable fits for the C IV line. Fits to the other lines, choosing the line ratio to match the observed ratio, are shown in the figure along with their χ^2 values and the number of points in the observed spectrum included in the calculation of χ^2. The observed spectrum has a number of
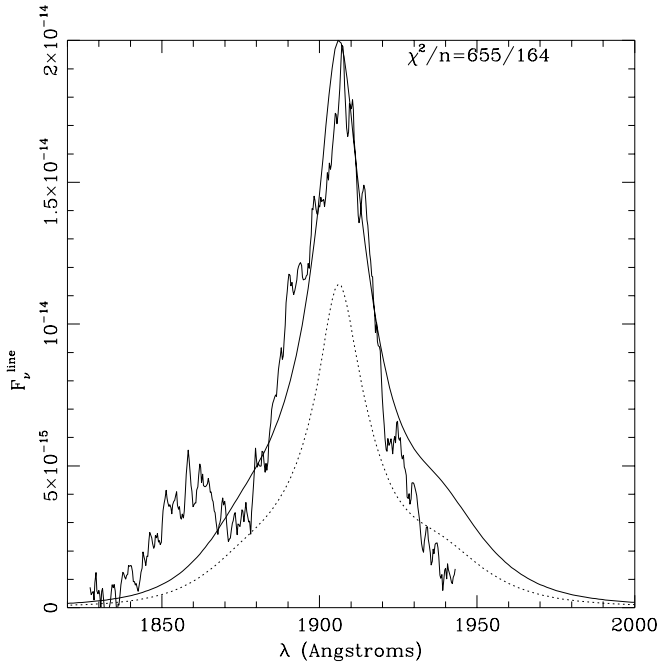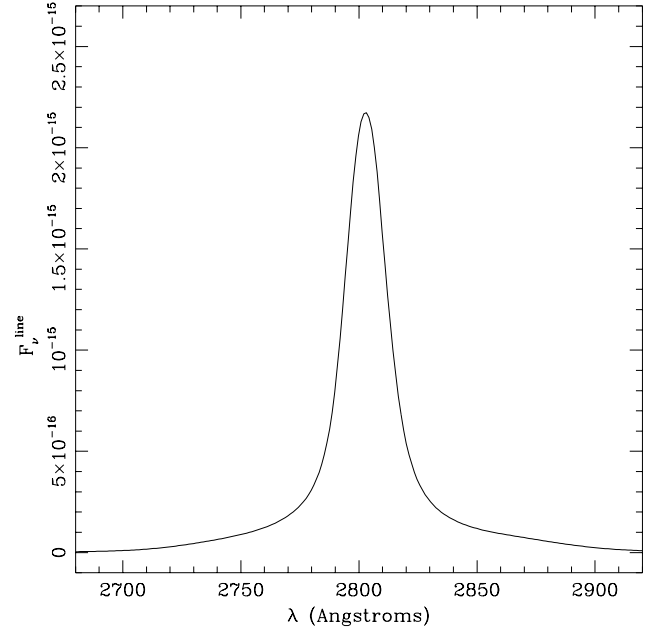
FIG. 6e

FIG. 6f

narrow absorption features. These are presumably caused by gas between us and the quasar. We have left out those portions of the lines affected by this absorption in the calculation of χ^2.

The observed C IV and Lyα lines have more blue emission than the calculated profiles. Some of the excess Lyα emission may be caused by C III* λ1176, as suggested by Laor et al. (1995). We have not attempted to fit this line. The rest of the excess Lyα and the excess C IV are possibly caused by resonantly scattered light, as predicted by the disk-wind model (MCGV) but are not included in our present calculations. The O VI profile is badly cut up by narrow absorption lines, but the fit is plausible. The excess emission on the blue side of the λ1909 feature we attribute to Al III λ1857 and Si III] λ1892 (Murray & Chiang 1997). The Mg II profile is far too narrow to explain the feature at λ2800. We discuss this below. The H$_\beta$ profile (not shown) resembles the Lyα profile, but we have no confidence in the prediction since we do not understand why the observed line ratio is so large. We find total Lyα fluxes that are very close to the observed

fluxes, but this is not a test of the model, since we adjust the break radius r_{break} to achieve the proper line flux. For example, in our PG 1116 model, we find a Lyα line flux of 476×10^{-14} ergs^{-1} s^{-1} cm^{-2} compared to a measured flux of 497×10^{-14} ergs^{-1} s^{-1} cm^{-2} (Laor et al. 1995).

We also show the Ne VIII profile predicted by the model, which is very broad, having a FWHM of $\sim 17,000$ km s^{-1}. We do not have any observational data for this line for either object. The dotted line in Figure 7a shows the effect of electron scattering, which might be important at the very smallest radii where the Ne VIII line forms (see the discussion in § 3). We assume that 25% of the Ne VIII photons are Thompson scattered. The effect is to increase the line width at zero intensity, although the effect on the overall line profile is not dramatic.

3.6. Mg II Emission

As can be seen from Table 3, the predicted Mg II flux is a factor of 3 smaller than the (possibly blended) flux found by Laor et al. (1995). Because of this, we have set the line flux in

TABLE 4

MODEL PARAMETERS

| Parameter	Fit or Fixed	PG 1634+706	PG 1116+215
L_{1350} (ergs s^{-1})	Fixed (observed)	1.5×10^{48}	10^{46}
M_{bh} ($M_\odot$)	Fit	4×10^{10}	3×10^8
Power-law index σ	Fit	2.75	2.5
Break radius r_{break} (cm)	Fit	3×10^{18}	3×10^{17}
Disk inclination (deg)	Fixed	60	60
Covering factor f	Fixed	0.10	0.10
Angle of incident radiation (deg)	Fixed	6	6
$\dot{M}_w(r)$	Fixed	$L/(2cv_\infty)$	$L/(2cv_\infty)$
λ (deg)	Fixed	10	10
Wind velocity exponent γ	Fixed	1.06	1.06
Wind scale height z_0	Fixed	$\dfrac{3\sigma_e L}{8\pi\eta c^3}$	$\dfrac{3\sigma_e L}{8\pi\eta c^3}$
Wind minimum velocity v_0 (cm s^{-1})	Fixed	10^{-6}	10^{-6}
Line flux relative to Lyα	Fit	...	...
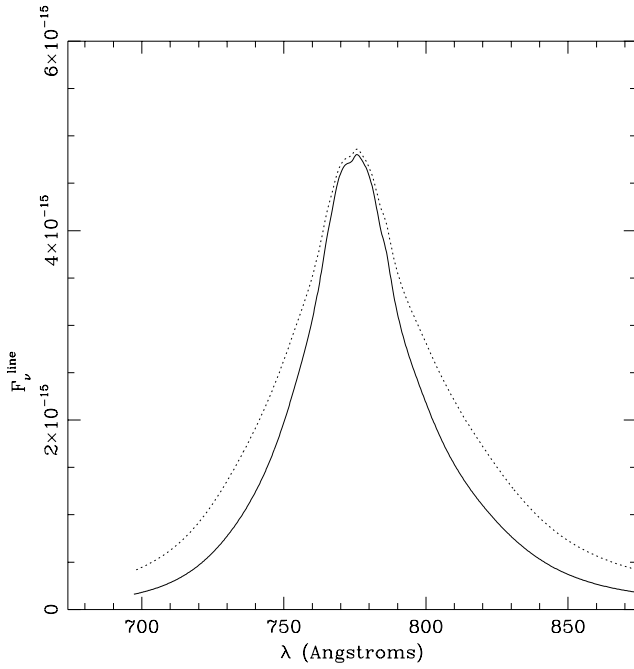
FIG. 7a
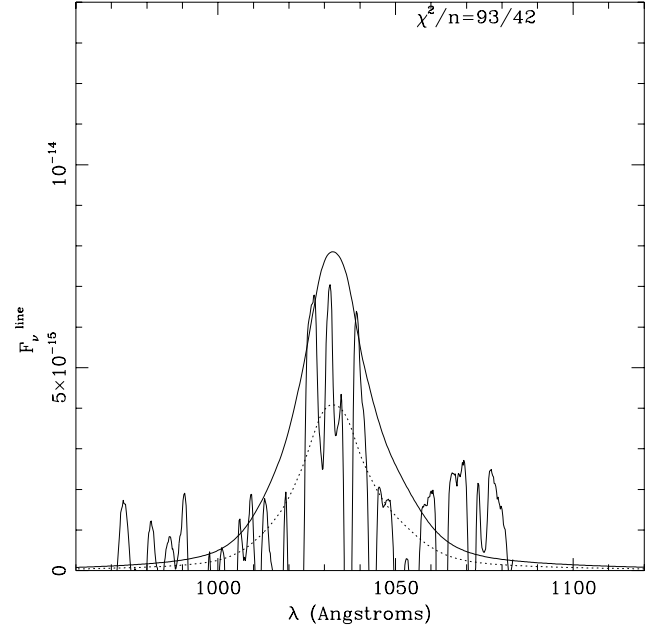
FIG. 7b

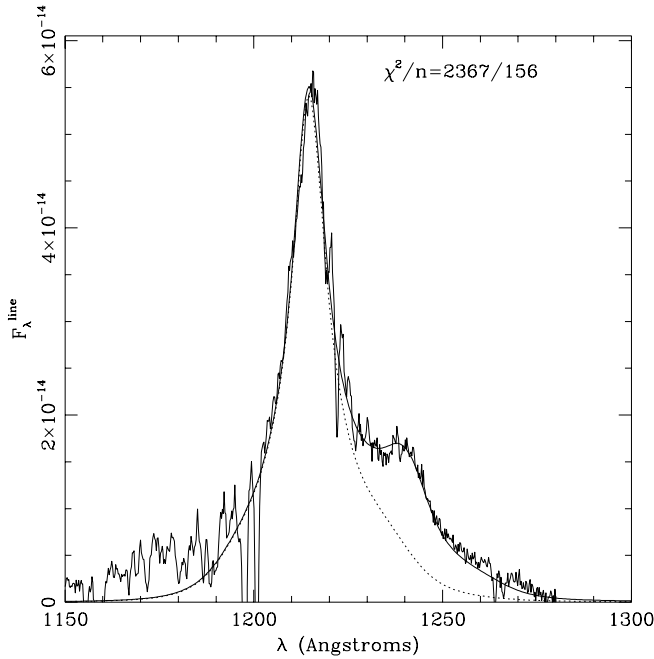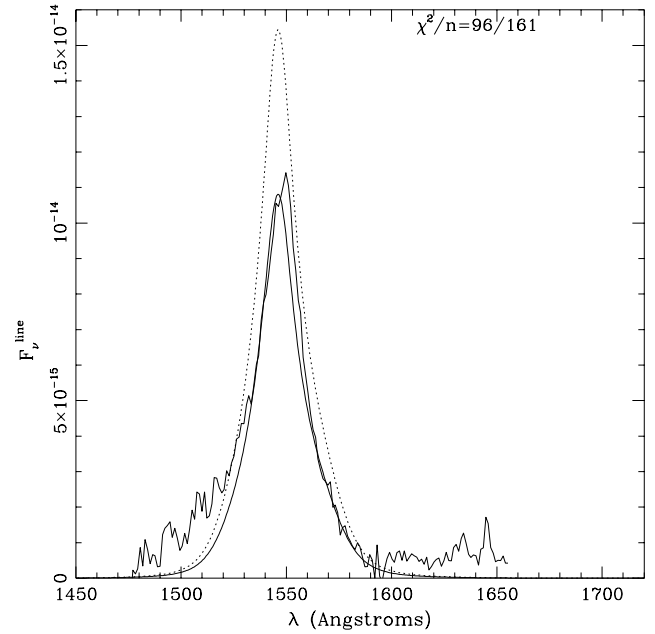
FIG. 7c

FIG. 7d

FIG. 7.—Line profiles generated by a source function with $\sigma = 2.75$ and $r_{break} = 3 \times 10^{18}$ (*dotted lines*), compared to the profiles observed in PG 1634+706 by Laor et al. (1995; *jagged solid lines*). The free parameters are the black hole mass ($4 \times 10^{10}\ M_\odot$, fixed by the full width at zero intensity of the C IV line), the break radius r_{break} (set by the flux of Lyα), the power-law slope σ (set by the FWHM of the C IV line), and, for the smooth solid line but not the dotted line, the peak intensity of each line or, equivalently for lines other than Mg II, the line ratio with Lyα. The χ^2 and number of points in the fit is shown in each panel.

the figure so that the peak intensity matches the observed peak intensity; the line ratio with Lyα is then ~0.03. The calculated Mg II line profile is much narrower than the observed profile in PG 1634+706, although it fits the core of the line well.

Mg II profiles often consist of two components, a narrow core and a much broader base, a fact noted by Steidel & Sargent (1991) in their large sample of quasar spectra. They fit both narrow and broad Gaussian components to their 74

Mg II profiles, finding a full width at half-maximum (FWHM) of 2850 ± 110 km s^{-1} for the narrow component and an FWHM of 13,100 ± 280 km s^{-1} for the broad component. The flux in the narrow component was only 0.37 ± 0.02 times the flux in the broad component, similar to the flux ratio in PG 1634+706. Steidel & Sargent (1991) concluded, on the basis of a good match between the velocity centroids of the narrow and broad Gaussian components, that the broad emission was caused by Mg II and
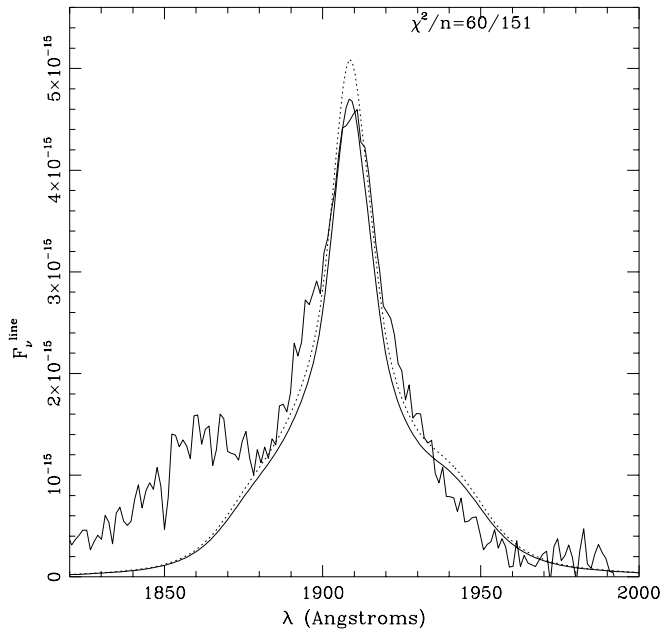
FIG. 7e

FIG. 7f

not contamination by Fe II emission. On the other hand, Wills, Netzer, & Wills (1985) suggested that the feature at 2800 Å was actually dominated by Fe II emission. Our results support the latter position.

As noted above, the bulk of the Mg II emission takes place at a large radius and deep in the wind, where the gas is moving subsonically. The emission length l_{em} is comparable to the Sobolev length l_S. More importantly, the velocity gradient $dv/dr \lesssim v_\phi/r$, so that the emission is essentially that of a Keplerian disk with no wind. It is only because the emission occurs at such large radii that the resulting profiles are single peaked. This is essentially the situation described by Collin-Souffrin and coworkers (see, e.g., Dumont & Collin-Souffrin 1990). We stress that, unlike the models of Collin-Souffrin, our models produce *all* the broad lines in the disk.

3.7. Ne VIII *and* Mg X *Emission and Absorption*

We find substantial Ne VIII emission, with intensity ranging from 0.02–0.2 as a fraction of Lyα emission. The line profile is very broad, as can be seen in Figures 6 and 7. The FWHM is $\sim 17,000$ km s^{-1}, with a FWZI of $\gtrsim 40,000$ km s^{-1}. Broad Ne VIII lines have been detected in *HST* spectra of moderate-redshift quasars (Hamann, Zuo, & Tytler 1995b) with strengths of 0.11–0.15 relative to Lyα. The profiles are very noisy but appear to be very broad; Hamann et al. (1995b) find an average FWHM of $11,160 \pm$ km s^{-1}, ranging up to $16,010 \pm 1415$ km s^{-1} in one object. They note that their detection implies gas in the broad-line region with $U > 5$. In our PG 1634 + 706 model, the gas that produces the Ne VIII emission sits at $r \approx 3 \times 10^{18}$ cm and has $U \approx 3000$! In that same model, the bulk of the C IV and Lyα emission comes from gas located at $r \sim 10^{19}$ cm that has $U = 0.2$.

As Hamann et al. (1995b) point out, their observations show that we still do not know the maximum ionization and temperature in the broad-line region. Moving toward shorter wavelengths, we note that the next Li-like ion reso-
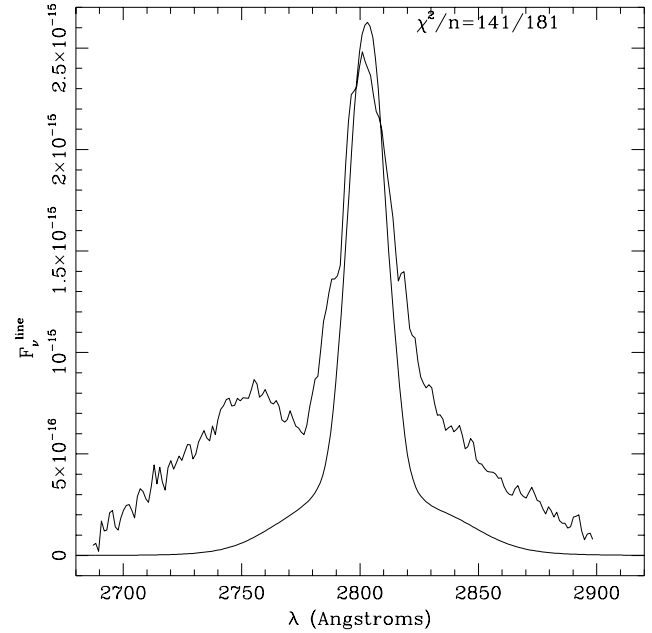
nance line is that of Mg X at 615 Å. Our predictions for the strength of this line are typically 0.0002 times that of Lyα. It is unlikely that the line can be detected in emission if these line strengths are correct.

The disk-wind model predicts that all the resonance lines seen in emission will also produce broad absorption lines in objects where the accretion disk is viewed nearly edge-on. Ne VIII has already been seen in absorption, albeit with only moderate width (Hamann et al. 1995a). While Mg X is unlikely to be found in emission, the optical depth of the line exceeds unity out to very large velocities in our models. As a result, we expect the Mg X line to produce broad absorption lines, a point made in MCGV. We suggest that observers look for both Ne VIII and Mg X in absorption in broad absorption line quasars.

4. DISCUSSION

Standard photoionization models for the broad-line region are described in the review by Netzer (Blandford et al. 1990). In the simplest form, these consist of an ensemble of identical clouds with a specified velocity distribution. The ionization parameter is chosen to give line ratios that match those observed, with moderate success. As with all photoionization models employing solar abundances (Hamann & Ferland 1993), Netzer's calculations underpredict the strength of N V and Hβ. The particular velocity distribution and the ionization parameter needed to match the observed line ratios and line profiles are left unexplained. Furthermore, since all the clouds are the same, the calculated profiles of different lines are very similar, in contrast to observed line profiles. More sophisticated models (Rees, Netzer, & Ferland 1989; Krolik et al. 1991; O'Brien, Goad, & Gondhalekar 1994) allow for a variety of clouds, subject to the constraint that the cloud pressure is a function of radius only.

More recently, Baldwin et al. (1995) have considered ensembles of random clouds, with a range of pressures, densities, and ionization parameters at a given distance from

the central source. They do not attempt a physical explanation for the range of gas properties. They find moderately good agreement (about as good as the classical models described in the last paragraph find) with observed line ratios. Their models underpredict N v and Hβ, as well as Si IV/O IV. They actually overpredict the strength of Mg II, even under the assumption that all the flux in the 2800 Å feature is caused by that ion. This is because they allow for emission from gas with U as small as 10^{-5} at a density of 10^{12} cm^{-3} but at very low column density (10^{23}). For a luminosity of 10^{46} ergs s^{-1}, this occurs at $r \approx 5 \times 10^{18}$ cm, where the Keplerian velocity is about 400 km s^{-1} for a black hole mass of $10^8 M_\odot$. If the cloud motion is virialized, the Mg II line in their model will be narrow.

The photoionization properties of the wind models described in this paper are very similar to those of Baldwin et al. (1995). In a wind, the emitting gas has a range of pressure, density, and ionization parameter at each radius. This is caused by the acceleration and lack of confinement of the gas, coupled with the continuity equation. Not surprisingly, we find line ratios that are similar to theirs. The one exception is the Mg II emission. There are two reasons for this. First, in the wind model, there is no emitting gas with a value of U as small as that considered by Baldwin et al. Second, where the wind does have a low ionization parameter, the column density is much larger than in the clouds Baldwin et al. (1995) consider; the larger overlying column ensures that the Mg II photons cannot easily escape from the wind. We agree with the general conclusion of Baldwin et al. that there is no fine tuning operating in the broad-line region.

The other type of photoionization model similar in approach to ours is the stellar wind model (Norman & Scoville 1988; Alexander & Netzer 1994). In this scenario, the line-emitting gas resides in the wind or extended envelope of a large number of giant stars. Alexander & Netzer carry out detailed photoionization calculations for both accelerating winds, in which velocity increases with increasing distance from each star, and for decelerating or nonaccelerating winds. The latter are very like classical clouds. The line ratios they find are similar to ours. In particular, their models underpredict both N v and Mg II. As in the disk-wind model, Mg II is underproduced because regions where U is low occur at large column densities. The Mg II emission occurs at large distances from the black hole, suggesting that the Mg II line should be narrow, although they do not calculate any line profiles.

Their models tend to overpredict the broad component of the forbidden lines, particularly in accelerating winds. We do not find such strong forbidden line emission in our models. One possible reason for the discrepancy is the difference in geometry of a disk wind versus a stellar wind, a point noted by Alexander & Netzer. In a spherical wind, the emitting volume tends to be dominated by the outer, less dense portion of the wind, where the forbidden emission is strong. Some of their models, namely those with decelerating or nonaccelerating low-velocity ($v < 10$ km s^{-1}) winds, avoid the forbidden line problem. However, such slow-wind models can be distinguished from disk-wind models by examining the broad line profiles. Stellar wind models with slow winds necessarily produce discreet components in the line profiles, since only $\sim 10^5$ giant stars can fit into the broad-line region without colliding on short timescales. Searches for such line structure may be able to

rule out stellar wind models (N. Arav 1996, private communication).

4.1. *Reverberation Mapping*

Reverberation mapping can be used to place constraints on the radius at which a given line is formed. The idea is to measure the time lag between a change in the continuum and the corresponding change in the emission lines. The method assumes that the lines are powered by the ionizing continuum beyond the Lyman edge and that the continuum longward of the edge, which is what is observed, closely tracks the ionizing continuum. The size of the time lag then gives some measure of the distance of the broad-line region from the continuum source.

So far, the technique has been applied only to low-luminosity AGNs (Seyfert galaxies), but we expect that qualitatively similar results will apply to quasars. Observations of Seyferts strongly suggest that the broad-line region is stratified, in the sense that high-ionization lines show small lags while low-ionization lines show much longer lags. For example, Korista et al. (1995) examined NGC 5548, finding a line-continuum cross-correlation time lag of ~1.5 days for He II and N v, 4.6 days for C IV, and 11 days for Hβ. This suggests that Mg II, which Korista et al. do not measure, should have a large lag and so presumably should form at large radii. In earlier campaigns on the same object, but with poorer time resolution, Krolik et al. (1991) found somewhat longer lags for the same lines (4 days for He II and N v and 8 days for C IV), probably reflecting the time interval between observations. They find a lag for the Mg II/Fe II blend of 72 days, a factor of 9 larger than the lag they found for C IV and a factor of 18 longer than that found for C IV by Korista et al. The interpretation of these lags is difficult, but the very long Mg II lag strongly suggests that the Mg II/Fe II emission occurs at much larger radii than that of the high-ionization lines.

We have run models for NGC 5548 using the continuum in Krolik & Kriss (1996), assuming a luminosity of 10^{44} ergs s^{-1}. The formation radii of the lines are $\sim 10^{15.5}$ cm for Ne VIII and N v, $\sim 10^{16}$ cm for He II and O VI, $\sim 10^{16.5}$ cm for C IV and Lyα, and $\sim 10^{17}$ cm for Mg II. The inner edge of the wind is at 10^{15} cm. These results are qualitatively consistent with the reverberation results.

For our quasar model (PG 1116+215, $L \approx 10^{46}$ ergs s^{-1}) the radii at which the lines form are as follows: $r \approx \sim 10^{16}$ cm for Ne VIII, $\sim 3 \times 10^{16}$ cm for He II, O VI, and N v, $\sim 10^{18}$ cm for C IV and Lyα, and $\sim 10^{19}$ cm for Mg II. The inner edge of the wind is at $\sim 5 \times 10^{15}$ cm (MCGV). Future reverberation campaigns may be able to test these results.

5. CONCLUSIONS AND FUTURE WORK

We have described the results of photoionization calculations of the line emission from a self-illuminated accretion disk. The results take the form of line ratios, line profiles, and radii of line formation for a number of prominent emission lines. The agreement found between the calculated and observed line ratios is similar to that found for other photoionization calculations—that is to say, it is moderately good. Low-ionization lines such as Hβ and Si IV are underpredicted. The flux of Mg II is badly underpredicted relative to the emission observed between 2700 and 2900 Å. We suggest that some of this emission is actually caused by Fe II. The flux of the high-ionization line N v is also underpredicted; this may indicate that the abundance of N is

enhanced in AGNs. The model predicts significant Ne VIII emission, but the emission due to Mg X should be negligible in most quasars. Emission due to forbidden lines is also negligible, in agreement with observations.

Our calculated line profiles are shown in Figures 6 and 7, together with the emission lines of PG 1116+215 and PG 1643+706. In fitting the C IV profile, we have treated the mass of the black hole, the slope of the power law (σ), the radius r_{break} of the break in the power law, and the intensity at line center as free parameters. The other lines were then fit with the first three parameters fixed but the intensity at line center allowed to vary. The calculated profiles are in good agreement with the observed profiles. The only exception is the Mg II line, for which the calculated profile is much narrower than the observed profile. As noted above, we attribute the broad base of the feature at 2700 Å to Fe II emission. This claim may be checked by reverberation studies measuring the lag of the Mg II line.

The disk-emission model predicts that the Ne VIII line will have a very broad profile (FWHM), partly because of the large doublet spacing but primarily because of the very small formation radius. Spaced-based observations of moderate-redshift quasars will be able to test this prediction. Ne VIII should also be seen in absorption.

Line emission from Mg X is likely to be undetectable, but the model predicts that the optical depth to scattering exceeds unity out to very large wind velocities. We therefore predict that Mg X will produce broad absorption lines and urge observers to look for it in spectra of broad absorption line quasars that extend far enough to the blue.

Figure 5 shows that high-ionization lines form at smaller radii than do low-ionization lines in our model quasars. This is qualitatively consistent with reverberation mapping observations of low-luminosity AGNs. In earlier work, we have shown that the predictions of a disk-wind model for the C IV line of NGC 5548 are in good agreement with the observed behavior of that line (Chiang & Murray 1996). We leave quantitative comparisons with this and other lines for later work.

Figure 3 shows that high-ionization lines are emitted by gas having a substantial radial and vertical velocity. In our calculations of the line profiles, we have assumed that the nonazimuthal velocity is zero. It is clear that relaxing this assumption will lead to blueshifts of the line centers. These shifts will be larger for higher ionization lines. Resonance scattering by the wind, which we have neglected, will also tend to produce blue asymmetries in resonance lines since the disk blocks the light from the wind on the side opposite the observer. It is straightforward to account for the nonzero wind velocity of the emitting gas, but accounting for the resonance scattering requires a better solution for the wind, which we leave for later work. We note that while Laor et al. (1995) found no evidence for any blueshifts in PG 1634+706, there is some observational evidence that high-ionization lines are systematically blueshifted relative to low-ionization lines (Tytler & Fan 1992) in many quasars.

REFERENCES

Alexander, T., & Netzer, H. 1994, MNRAS, 270, 781
Baldwin, J., Ferland, G., Korista, K., & Verner, D. 1995, ApJ, 455, 119
Beuermann, K., & Thomas, H.-C. 1990, A&A, 230, 326
Blandford, R. D., Netzer, H., & Woltjer, L. 1990, Active Galactic Nuclei, Saas-Fee Lecture Notes 20 (Berlin: Springer)
Boroson, B., Vrtilek, S. D., McCray, D., Kallman, T., & Nagase, F. 1996, ApJ, 473, 1079
Chiang, J., & Murray, N. 1996, ApJ, 466, 704
Dumont, A. M., & Collin-Souffrin, S. 1990, A&A, 229, 313
Ferland, G. J. 1993, University of Kentucky Department of Physics and Astronomy Internal Report
Hamann, F., Barlow, T. A., Beaver, E. A., Burbidge, E. M., Cohen, R. D., Junkkarinen, V., & Lyons, R. 1995a, ApJ, 443, 606
Hamann, F., & Ferland, G. 1993, ApJ, 418, 11
Hamann, F., Zuo, L., & Tytler, D. 1995b, ApJ, 444, 69
Herrnstein, J. R., Greenhill, L. J., & Moran, J. M. 1996, ApJ, 468, 17
Horne, K. 1995, A&A, 297, 273
Iwasawa, K., et al. 1996, MNRAS, 282, 1038
Korista, K., et al. 1995, ApJS, 97, 285
Krolik, J. H., Horne, K., Kallman, T. R., Malkan, M. A., Edelson, R. A., & Kriss, G. A. 1991, ApJ, 371, 541
Krolik, J. H., & Kriss, G. A. 1996, ApJ, 456, 909
Laor, A., Bahcall, J. N., Jannuzi, B. T., Schneider, D. P., & Green, R. F. 1995, ApJS, 99, 1

Marsh, T. R., & Horne, K. 1990, ApJ, 349, 593
Mathews, W. G., & Ferland, G. J. 1987, ApJ, 323, 456
Miyoshi, M., Moran, J. M., Herrnstein, J. R., Greenhill, L. J., Nakai, N., Diamond, J. J., & Inoue, M. 1995, Nature, 373, 127
Murray, N., & Chiang, J. 1996, Nature, 382, 789
———. 1997, ApJ, 474, 91
Murray, N., Chiang, J., Grossman, S., & Voit, G. M. 1995, ApJ, 451, 498
Norman, C., & Scoville, N. 1988, ApJ, 332, 124
O'Brien, P. T., Goad, M. R., & Gondhalekar, P. M. 1994, MNRAS, 268, 845
Rees, M. J., Netzer, H., & Ferland, G. J. 1989, ApJ, 347, 640
Shakura, N. I., & Sunyaev, R. A. 1973, ApJ, 24, 337
Steidel, C. C., & Sargent, W. L. W. 1991, ApJ, 382, 433
Tanaka, Y., et al. 1995, Nature, 375, 659
Tytler, D., & Fan, X.-M. 1992, ApJS, 79, 1
Welty, A. D., Strom, S. E., Edwards, S., Kenyon, S. J., & Hartmann, L. W. 1992, ApJ, 397, 260
Wills, B. J., Netzer, H., & Wills, D. 1985, ApJ, 288, 94
Young, P., Schneider, D. P., & Shectman, S. A. 1981, ApJ, 245, 1035
Zheng, W., Kriss, G. A., Telfer, R. C., Grimes, J. P., & Davidsen, A. F. 1997, ApJ, 475, 469